Layer and doping tunable ferromagnetic order in two-dimensional CrS_2 layers

Cong Wang,[1] Xieyu Zhou,[1] Yuhao Pan,[1] Jingsi Qiao,[1] Xianghua Kong,[1] Chao-Cheng Kaun,[2] and Wei Ji[1,*]

[1]*Beijing Key Laboratory of Optoelectronic Functional Materials & Micro-Nano Devices, Department of Physics, Renmin University of China, Beijing 100872, People's Republic of China*

[2]*Research Center for Applied Sciences, Academia Sinica, Taipei 11529, Taiwan, Republic of China*

(Received 22 February 2018; revised manuscript received 20 May 2018; published 12 June 2018)

Interlayer coupling is of vital importance for manipulating physical properties, e.g., electronic band gap, in two-dimensional materials. However, tuning magnetic properties in these materials is yet to be addressed. Here, we found the in-plane magnetic orders of CrS_2 mono and few layers are tunable between striped antiferromagnetic (sAFM) and ferromagnetic (FM) orders by manipulating charge transfer between Cr t_{2g} and e_g orbitals. Such charge transfer is realizable through interlayer coupling, direct charge doping, or substituting S with Cl atoms. In particular, the transferred charge effectively reduces a portion of Cr^{4+} to Cr^{3+}, which, together with delocalized S p orbitals and their resulting direct S-S interlayer hopping, enhances the double-exchange mechanism favoring the FM rather than sAFM order. An exceptional interlayer spin-exchange parameter was revealed over -10 meV, an order of magnitude stronger than available results of interlayer magnetic coupling. It addition, the charge doping could tune CrS_2 between p- and n-doped magnetic semiconductors. Given these results, several prototype devices were proposed for manipulating magnetic orders using external electric fields or mechanical motion. These results manifest the role of interlayer coupling in modifying magnetic properties of layered materials and shed considerable light on manipulating magnetism in these materials.

DOI: 10.1103/PhysRevB.97.245409

I. INTRODUCTION

Geometric, electronic, vibrational, thermal, and optical properties of layered two-dimensional (2D) materials, such as graphene [1–4], transition-metal dichalcogenides (TMDs) [5–9], and black phosphorus (BP) [10–15], have received considerable attention in the past decade. Magnetic properties were, however, rarely mentioned and are thus of particular interest. Magnetism in 2D materials could be introduced by dosing adatoms [16–20], atom substitution [21], creating vacancies [16,22] or boundaries [23], or constructing atomic edges [24,25]. Nevertheless, the long-range magnetic ordering was argued less stable in 2D because of the largely reduced size in the perpendicular direction according to the Mermin-Wagner theorem [26]. Therefore, the long-range ordering could be easily eliminated by thermal fluctuation, leading a ferromagnetic (FM) or antiferromagnetic (AFM) to paramagnetic transition. It was very recently reported that magnetic ordering persists even if the thickness is down to monolayer in CrI_3 [27,28]. Another strategy relies on a magnetic exchange field that stabilizes the long-range ordering with magnetic anisotropy in a bilayer $Cr_2Ge_2Te_6$ [29]. These two studies compellingly support the existence of long-range magnetic ordering in 2D, which may allow surface-sensitive techniques to measure 2D magnets and improve the feasibility of theoretical models built in 2D for real materials under investigation. However, the knowledge of manipulating magnetism in 2D is yet to be revealed.

Interlayer coupling has been manifested to be of paramount importance in manipulating physical properties [4,13,14,30–35] in 2D materials. The layer tunability is a result of layer-dependent electronic structures caused by strong interlayer electronic coupling, named covalentlike quasibonding (CLQB) [14,32,36,37]. In CLQB-governed 2D layers, the distance between two or more layers is pushed close enough by the van der Waals attraction that the wave functions, especially from p_z or d_{z^2} orbitals, of two adjacent layers are forced to overlap, forming bonding and antibonding states. Such hybridization should substantially modify electron distributions in both layers and thus may change either in-layer or interlayer magnetic coupling. As evidenced by the layer-dependent interlayer magnetic orderings in CrI_3, interlayer coupling might play an essential role in tuning interlayer magnetism. However, its ability of varying *in-plane* magnetic ordering is neither theoretical suggested or experimentally proved. The interlayer engineering [38] aside, charge doping by, e.g., ionic liquid gating, has been becoming a popular route to manipulate electronic properties in 2D. A recent work reported an O^{2-}-ion-doping–induced change of magnetism in $Co/SrCoO_x$ thin films [39]. Nevertheless, the O atom itself, rather than the charge solely, plays a key role. It still lacks an example for a purely electron- or hole-doping governed transition of in-layer or interlayer magnetic orders in layered materials.

In this article, we report a theoretical investigation on the layer- and doping-dependent magnetism in CrS_2 few layers. Monolayer CrS_2 is in a striped antiferromagnetic order (sAFM) [40–43]. It undergoes a sAFM-to-FM transition if one or more additional layers is stacked onto the monolayer. Such a transition is a result of a strong interlayer CLQB, which weakens the in-plane Cr-S σ bonds and transfers electrons from e_g to

*wji@ruc.edu.cn

partially occupied t_{2g} orbitals of Cr. It is exceptional that the interlayer spin-exchange coupling parameter of −10.8 meV is nearly an order of magnitude larger than previously reported values in other materials [29,44,45]. Layer stacking aside, we also discussed the roles of sole electron or hole doping or elemental substitution [46,47] in tuning magnetism in 2D. These results suggest CrS_2 is a FM/sAFM switchable 2D layer and illustrate the ability of interlayer engineering for tuning either in-layer or interlayer magnetism in layered magnets.

II. METHODOLOGY

A. Density functional theory calculations

Density functional theory calculations were performed using the generalized gradient approximation for the exchange-correlation potential, the projector augmented wave method [48], and a plane-wave basis set as implemented in the Vienna ab-initio simulation package (VASP) [49]. The energy cutoff for plane waves of 700 and 600 eV was adopted for calculation of structural relaxation and electronic structures, respectively. A $16\times10\times1$ k mesh was used to sample the first Brillouin zone of the adopted $1\times\sqrt{3}\times1$ rectangular supercell. A second-order Methfessel-Paxton smearing method (with a σ value of 0.1 eV) and a Bloch-corrected tetrahedron method were used for structural relaxations and total energy calculations, respectively. Dispersion correction was made at the van der Waals density functional (vdW-DF) level, with the optB86b functional for the exchange potential [50]. All atoms in the supercell were allowed to relax until the residual force per atom was less than 0.01 eV/Å. A 2 ×4 supercell was adopted to calculate the exchange parameters. All configurations were fully relaxed.

B. DFT+U method

The DFT+U method considers orbital dependence of the Coulomb and exchange interactions, which gives a qualitative improvement compared with standard DFT to transition-metal systems for either magnetic moments or interatomic exchange parameters [51]. Here, the adopted value was suggested from the literature [52] where a U value of 0.26 Ry and a J value of 0.053 Ry, equivalent to an effective U value of approximately 2.8 eV, was unveiled in systems of Cr impurities embedded in metal. Since CrS_2 is metallic, the Coulomb screenings in both cases shall be comparable and the choice of 2.8 eV is thus reasonable for describing the on-site U effect in CrS_2.

We have also self-consistently calculated the U value using a linear response method [53]. The calculated U value is in a range from 1.5 to 2.5 eV, close to the value reported in the literature (from 2 to 4 eV) [52,54–57] and the value we adopted (2.8 eV). In addition, we checked several effective U values (Supplemental Material, Fig. S1 [58]) and found it is robust to show the found large interlayer exchange coupling parameter and the doping-induced sAFM-FM transition. The choice of 2.8 eV is thus reasonable for describing the on-site U effect in CrS_2.

The experimental ground state of $CrSe_2$, an analog compound of CrS_2, is magnetic [59,60]. A 2H nonmagnetic ground state of $CrSe_2$ was unveiled in our calculations without a U term (0.20 eV more stable than the 1T-sAFM state). If we consider the U term, an 1T-sAFM ground state was compellingly suggested with the U value varying from 1 to 5 eV (over 0.41 eV more stable for $U = 2.8$ eV). Given the experiment magnetic ground state, it thus indicates the U term is paramount for obtaining the correct ground state of Cr chalcogenides using state-of-the-art DFT methods.

The agreement of our results with the experiments aside, a previous calculation [61] also reported the 1T magnetic ground state of $CrSe_2$ using a localized spherical wave (LSW) method. This method assumes spherical tight-binding wave functions and fills the space of the lattice using occupied or empty spheres and predicted the magnetic ground state without U. Here, the choices of sphere positions/types and the radii of spheres are all parameters to be determined or fitted. In light of this, we thus have confidence that our DFT+U method is a state-of-the-art method for modeling Cr dichalcogenides.

C. Carrier mobility estimation

Phonon-limited carrier mobility in a CrS_2 few layer with a finite thickness W_{eff} is expressed as [62–65]

$$\mu_{\text{film}} = \frac{\pi e\hbar^4 C_{\text{film}}}{\sqrt{2}(k_B T)^{3/2}(m^*)^{5/2}\left(E_1^i\right)^2} F$$

Here, m^* represents the effective mass along the transport direction and E_1 is the deformation potential constant of the valence band or conduction band maximum [VBM (hole) or CBM (electron), respectively] along the transport direction, which is determined by $E_1^i = \Delta V_i/(\Delta l/l_0)$. Here ΔV_i is the energy change of the ith band under proper cell compression and dilatation (by a step 0.5%), l_0 is the corresponding lattice constant along the transport direction, and Δl is the deformation of the lattice constant. The variable C_{film} is the elastic modulus of the longitudinal strain in the propagation direction, which is derived by $(E - E_0)/V_0 = C(\Delta l/l_0)^2/2$; E represents the total energy and V_0 represents the lattice volume at the equilibrium for 2D systems. A crossover function F bridges the 2D and 3D cases, which is estimated by

$$F \equiv \frac{\sum_n \left\{\frac{\sqrt{\pi}}{2}\{1 - \text{erf}[\Omega(n)]\} + \Omega(n)e^{-\Omega^2(n)}\right\}}{\sum_n \left[1 + \Omega^2(n)\right]e^{-\Omega^2(n)}},$$

where

$$\Omega(n) \equiv \sqrt{\frac{n^2\pi^2\hbar^2}{2m^* W_{\text{eff}}^2 k_B T}},$$

erf(·) represents an error function, and the summation over integer is due to quantum confinement along the z direction. The effective thickness of the film (W_{eff}) is expressed by

$$\frac{1}{W_{\text{eff}}} = \int_{-\infty}^{+\infty} P_i(z)P_f(z)dz = \sum_n \frac{\rho_i^n(z)}{N\Delta z}\frac{\rho_i^n(z)}{N\Delta z}\Delta z.$$

Here, $P(x)$ is the electron probability density along the z direction. We divided the space along the x direction into n parts by Δz. Variable $\rho^n(z)$ is the sum of the number of electrons in the nth region along the z direction. Here, N is the total number of valence electrons in the film, and i and f represent equilibrium and deformed films, respectively.

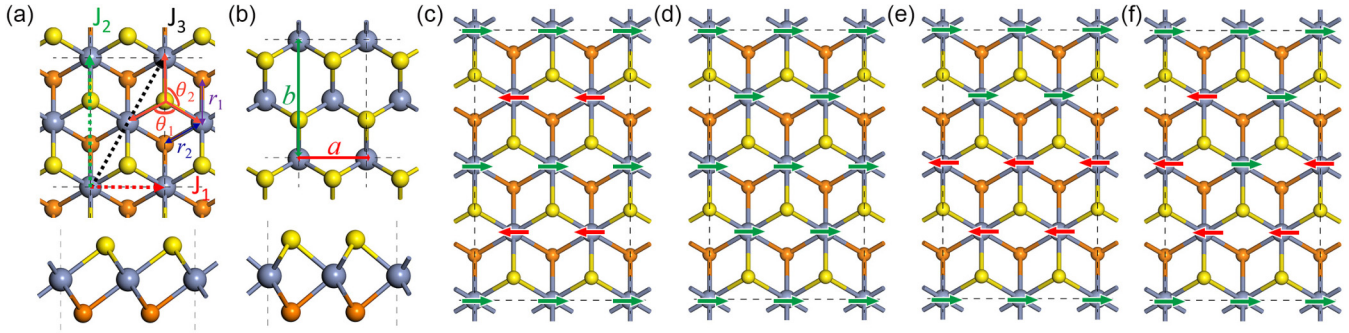

FIG. 1. Schematic models of monolayer CrS_2 and four different magnetic orders. (a), (b) Top and side view of single-layer CrS_2 in 1T (a) and 2H (b) phase. The slate-blue, yellow, and orange balls represent Cr, top S, and bottom S atoms, respectively. The intralayer spin-exchange parameters J_1, J_2, J_3 between Cr sites are represented with dashed arrows. The red, green, blue, and purple arrows correspond to lattice constants a and b, Cr-S bond r_1 and r_2. The two red arcs represent the Cr-S-Cr angles θ_1 and θ_2, respectively. (c)–(f) Schematic representation of four intralayer magnetic orders used for calculation of exchange parameters. The green and red arrows represent the magnetic moment up and down on Cr atoms, respectively.

D. Plotted charge densities

The spin charge density shows the distribution of charge with different spin components. Two sets of data, total charge density (spin up plus spin down) and magnetization density (spin up minus spin down), are available in spin-polarized calculations. The charge density with the spin-up (-down) component can be extracted by adding (subtracting) the two sets of data. The atomic differential charge density was plotted to show the charge redistribution before and after Cr and S atoms forming a CrS_2 monolayer, which is determined by $\Delta\rho_a = \rho_0 - \rho_a$. Here ρ_0 is the charge density converged in an electronic self-consistency loop which contains the interaction between bonded atoms, while ρ_a is obtained by a non-self-consistent calculation for summing over atomic charge densities.

E. Implementation of charge doping

Direct charge doping was applied on S atoms with the ionic potential method [66] to tune magnetic orders and to understand the role of interlayer couplings. Electrons (holes) are removed from a $2p$ core level of S and placed into the lowest unoccupied band of CrS_2. This method ensures the doped charges being located around the S atom and keeps the neutrality of the layer. We also plotted the differential charge density of doped systems using $\Delta\rho_d = \rho_d - \rho_0$, where ρ_d is the charge density of a doped CrS_2.

F. Interlayer force constant

The whole layer is regarded as one rigid body in a rigid-layer vibrational mode [32,67]. The interlayer force constants were obtained by summing interatomic force constants over all atoms from each of the two adjacent layers. The matrix of interatomic force constants, essentially the Hessian matrix of the Born-Oppenheimer energy surface, was defined as the energetic response to a distortion of atomic geometry in DFPT [68], which reads as $D_{ij} = \frac{\partial^2 E(R)}{\partial R_i \partial R_j}$. Here, R is the coordinate of each atom and $E(R)$ is the ground-state energy.

III. RESULTS AND DISCUSSION

A. Structure and spin-exchange coupling of monolayer CrS_2

A striped antiferromagnetic state in the 1T phase [1T-sAFM, see Figs. 1(a) and 1(c)] is the most energetically favored (over 23 meV/Cr) state of a monolayer CrS_2, rather than the previously believed nonmagnetic 2H phase [2H-NM, Fig. 1(b) and Supplemental Fig. S2] [40–43]. The sAFM ground state persists under six different U values (1−5 eV, Supplemental Fig. S1a [58]). The magnetic moment of each Cr atom slightly depends on the adopted magnetic order in a range from 2.4 to 2.8 μ_B. These moments reduce by 0.6–0.8 μ_B if the U term is not considered (Supplemental Table S1 [58]). The formation of magnetic stripes reduces the threefold structural symmetry that a Jahn-Teller distortion occurs in the sAFM configuration, namely, $a = 3.31$ Å, $b = 5.45$ Å, $r_1 = 2.38$ Å, and $r_2 = 2.36$ Å, $\theta_1 = 88.2°$, $\theta_2 = 84.6°$. The smaller θ_2 prefers to weaken Hund's law and thus favoring AFM coupling. In FM [Fig. 1(d)], however, the symmetry is maintained and θ_2 approaches 90° (87.7°), resulting in a shrunk by 0.02 Å and b expanded by 0.25 Å.

Spin-exchange coupling parameters were extracted based on a third-nearest Heisenberg model as follow:

$$H = H_0 + J_1 \sum_{\langle ij \rangle} \vec{S_i} \cdot \vec{S_j} + J_2 \sum_{\langle\langle ij \rangle\rangle} \vec{S_i} \cdot \vec{S_j} + J_3 \sum_{\langle\langle\langle ij \rangle\rangle\rangle} \vec{S_i} \cdot \vec{S_j}$$

Here, J_1, J_2, and J_3 represent the first-, second-, and third-nearest couplings, respectively, as illustrated in Fig. 1(a). Given the four configurations shown in Figs. 1(c)–1(f), we derived $J_1 = 47.7$ meV, $J_2 = -38.9$ meV, and $J_3 = 9.6$ meV. The larger $|J_1|$ than $|J_2|$ and the positive J_1 are consistent with the favored sAFM configuration.

B. Magnetic coupling mechanism of monolayer CrS_2

Figures 2(a) and 2(b) show the side and top views of the spin density of a CrS_2 monolayer in the sAFM configuration, which reflects the broken symmetry around S atoms. They also show localized S p_z densities for one spin component and delocalized p_x or p_y densities for the other spin component,

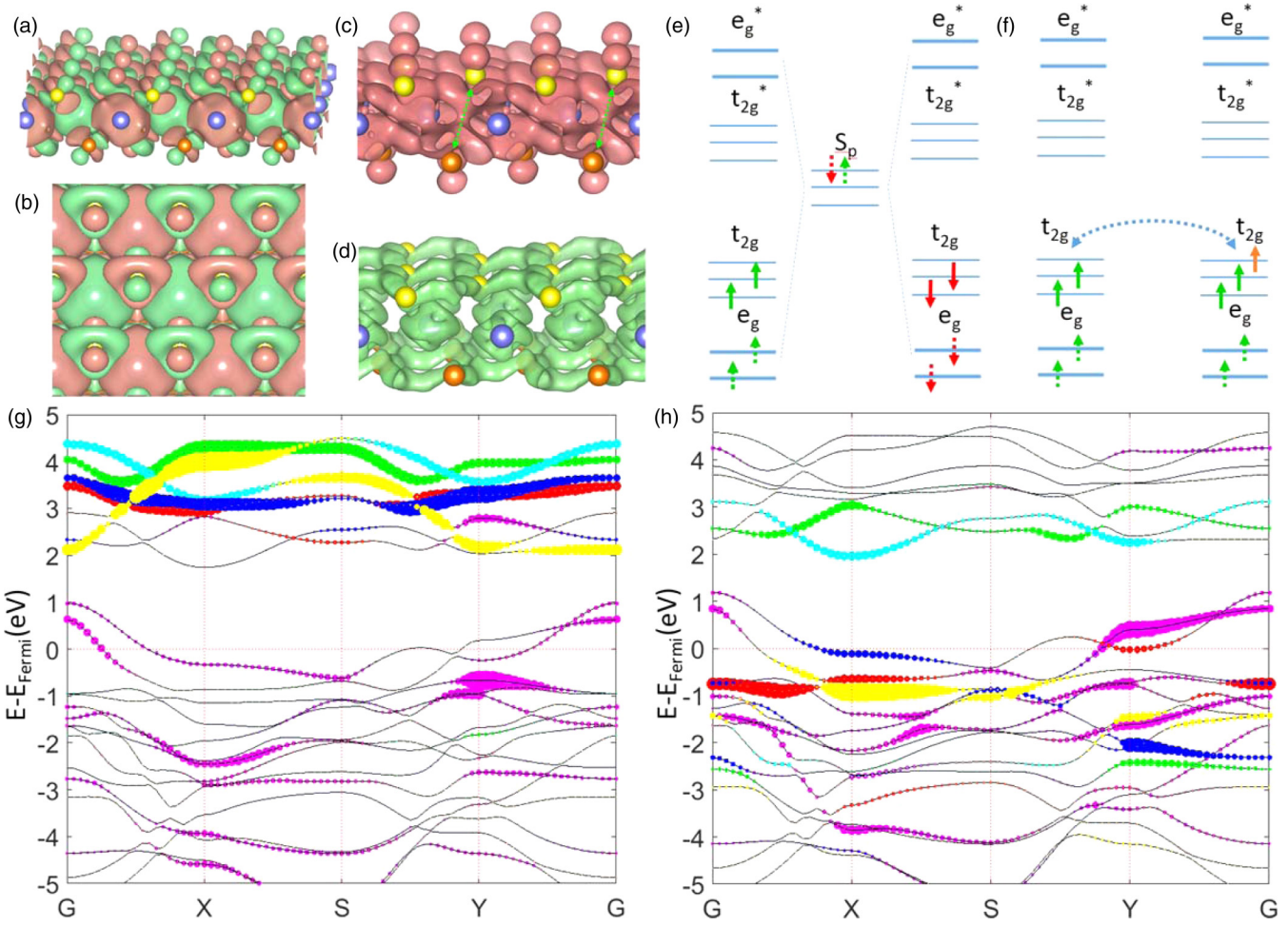

FIG. 2. Electronic structure of sAFM monolayer CrS_2. (a), (b) Spin charge density map of CrS_2 in sAFM order, side and top view. The red and green isosurface correspond to charge with different spin-polarized direction up and down. (c), (d) Atomic differential charge density of monolayer CrS_2, corresponding to the charge accumulation and reduction after Cr and S atoms bonding together, respectively. (e), (f) Schematics of superexchange and double-exchange mechanism for spin exchange between localized d electrons of Cr and itinerant electrons comprised of S p state and Cr d states. The up and down arrows represent the electron with different spin components and the dashed arrows correspond to bonding electrons from Cr and S atoms. The orange arrow in (e) indicates the transferred electrons from layer stacking or doping. (g), (h) Electronic band structure of the sAFM monolayer. CrS_2 with different spin component down (e) and up (f). The Fermi energy is zero. The Cr-d and S-p orbitals are mapped with different colors: Cr-d_{xy}, green; Cr-d_{yz}, red; Cr-d_{xz}, blue; Cr-d_{z^2}, cyan; Cr-$d_{x^2-y^2}$, yellow; S-p, magenta.

resulting a nearly canceled total magnetic moment of 0.034 μ_B. Atomic differential charge density of the monolayer depicts charge accumulation residing primarily around S atoms but varnishing around Cr atoms [Fig. 2(c)]. However, charge reduction [Fig. 2(d)] occurs mainly in the Cr $d_{x^2-y^2}$ and d_{z^2} orbitals and partially at the interatomic region of S atoms. An electron transfer is evidenced from S in-plane and Cr d e_g orbitals to out-of-plane S orbitals when forming the monolayer. These out-of-plane orbitals hybridize and develop pipelines connecting the S atoms in up and down layers, respectively, which builds an electron network for itinerant electrons. A superexchange coupling mechanism is thus suggested between two adjacent Cr atoms.

Here, Cr^{4+} adopts a p^3sd^2 hybridization that two e_g orbitals, i.e., $d_{x^2-y^2}$ and d_{z^2} are involved in forming σ bonds with S p orbitals. The two remaining d electrons are thus filled into three nearly degenerated t_{2g} orbitals [Fig. 2(e)], leading to a metallic CrS_2 monolayer with partially filled d_{xz} and d_{yz} orbitals [Figs. 2(g)–2(h)]. We may regard it as a highly p-doped semiconductor because of an unfilled bandgap of 0.77 eV sitting 1.1 eV above the Fermi Level (E_F). Orbital decompositions were mapped on the band structures [Figs. 2(g)–2(h)]. All five d orbitals are unoccupied and grouped together for the spin-down component; however, they split into two groups for the spin-up component. It confirms the p^3sd^2 hybridization picture and shows the σ bonding (~3 eV below E_F) and antibonding (~2 eV above E_F) states (green and cyan dots). Spins of the two d electrons filling the t_{2g} orbitals, together with back-donated electrons from the Cr-S σ bonds, are all parallel aligned [Fig. 2(e)] owing to the Hund's rule, which results in a local magnetic moment of 2.8 μ_B. Spin-orbit coupling does not qualitatively change the band structure but further splits the two spin components by 74 meV (Supplemental Fig. S3 [58]). The superexchange mechanism might be

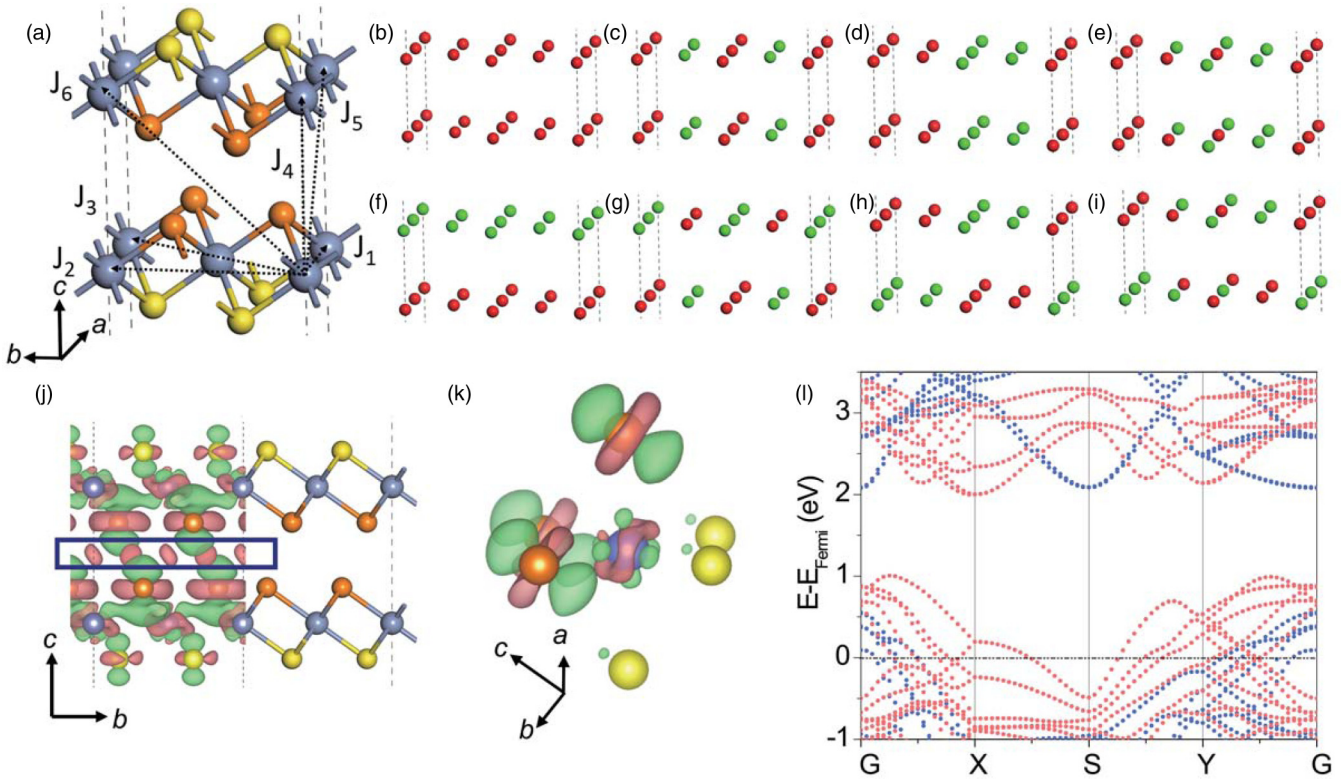

FIG. 3. Bilayer CrS_2. (a) Perspective view of AA-stacked bilayer CrS_2. Exchange parameters are marked with dashed arrows connected between Cr atoms. (b)–(i) Schematic representation of eight magnetic orders used for the calculation of exchange parameters in AA-stacked bilayer CrS_2. The green and red balls represent the magnetic moment up and down on Cr atoms, respectively. (j) Differential charger density (DCD) of bilayer CrS_2 with an isosurface value of 0.0005 e/Bohr^3. Light-rose and green isosurface indicates charge accumulation and depletion after layer stacking, respectively. (k) A zoomed-in plot around Cr atom of DCD of bilayer CrS_2 in (j). (l) Electronic band structure of the FM-FM bilayer CrS_2 with different spin components. Red: spin up; blue: spin down.

suppressed by transferring additional electrons into the t_{2g} orbitals. In that case, the mixed-valence states of Cr^{4+} and Cr^{3+} promote the double-exchange mechanism favoring a FM long-range ordering [Fig. 2(f)].

C. Manipulation of magnetic ordering by additional CrS_2 layers

Interlayer coupling of multilayers could redistribute charge density at the interlayer region [32,69]. We thus examined a CrS_2 bilayer shown in Fig. 3(a) where the AA stacking was found to be 0.34 eV more stable than the AB stacking (Supplemental Fig. S4 and Table S2 [58]). Spin-exchange coupling parameters [marked in Fig. 3(a)] were extracted by calculating the total energy differences of eight magnetic configurations [Figs. 3(b)–3(i)] based on the Heisenberg model. The energy contributed by magnetic interaction in these magnetic orders in a unit cell is expressed as

$$E_b = \frac{N^2}{4} \times \frac{1}{2}(6J_1 + 6J_2 + 6J_3 + J_4 + 6J_5 + 6J_6)$$

$$E_c = \frac{N^2}{4} \times \frac{1}{2}(-2J_1 + 6J_2 - 2J_3 + J_4 - 2J_5 - 2J_6)$$

$$E_d = \frac{N^2}{4} \times \frac{1}{2}(2J_1 - 2J_2 - 2J_3 + J_4 + 2J_5 - 2J_6)$$

$$E_e = \frac{N^2}{4} \times \frac{1}{2}(-J_1 + 2J_2 - J_3 + J_4 - J_5 + J_6)$$

$$E_f = \frac{N^2}{4} \times \frac{1}{2}(6J_1 + 6J_2 + 6J_3 - J_4 - 6J_5 - 6J_6)$$

$$E_g = \frac{N^2}{4} \times \frac{1}{2}(-2J_1 + 6J_2 - 2J_3 - J_4 + 2J_5 + 2J_6)$$

$$E_h = \frac{N^2}{4} \times \frac{1}{2}(2J_1 - 2J_2 - 2J_3 - J_4 - 2J_5 + 2J_6)$$

$$E_i = \frac{N^2}{4} \times \frac{1}{2}(-J_1 + 2J_2 - J_3 - J_4 + J_5 - J_6),$$

where N represents the unpaired spins on each Cr atom, which is treated as 2 in our exchange parameter calculations.

Here, the nearest interlayer parameter J_4 was derived -10.8 meV, considerably favoring FM, while J_1 and J_2 reduce to 16.3 meV and -19.4 meV, respectively. Nevertheless, another three parameters are negligible (<1 meV). It is exceptional that J_4 is over an order of magnitude larger than those of $Cr_2Ge_2Te_6$ [29], $RuCl_3$ [44], and MnI_2 [45], which is also robust under different U values, i.e. 2.0, 2.8, and 4.0 eV (see Supplemental Fig. S1b [58]). Unlike the monolayer case, the bilayer exceptionally undergoes a transition from the intralayer sAFM order in the monolayer to a both intra- and interlayer FM order, with at least 8 meV/Cr energy gain in bilayer and thicker layers (Supplemental Tables S2 and S3 [58]). This FM-FM configuration offers the shortest interlayer S-S distance of 3.18 Å, 0.04 Å smaller than the second-shortest distance among all configurations. After this transition, the

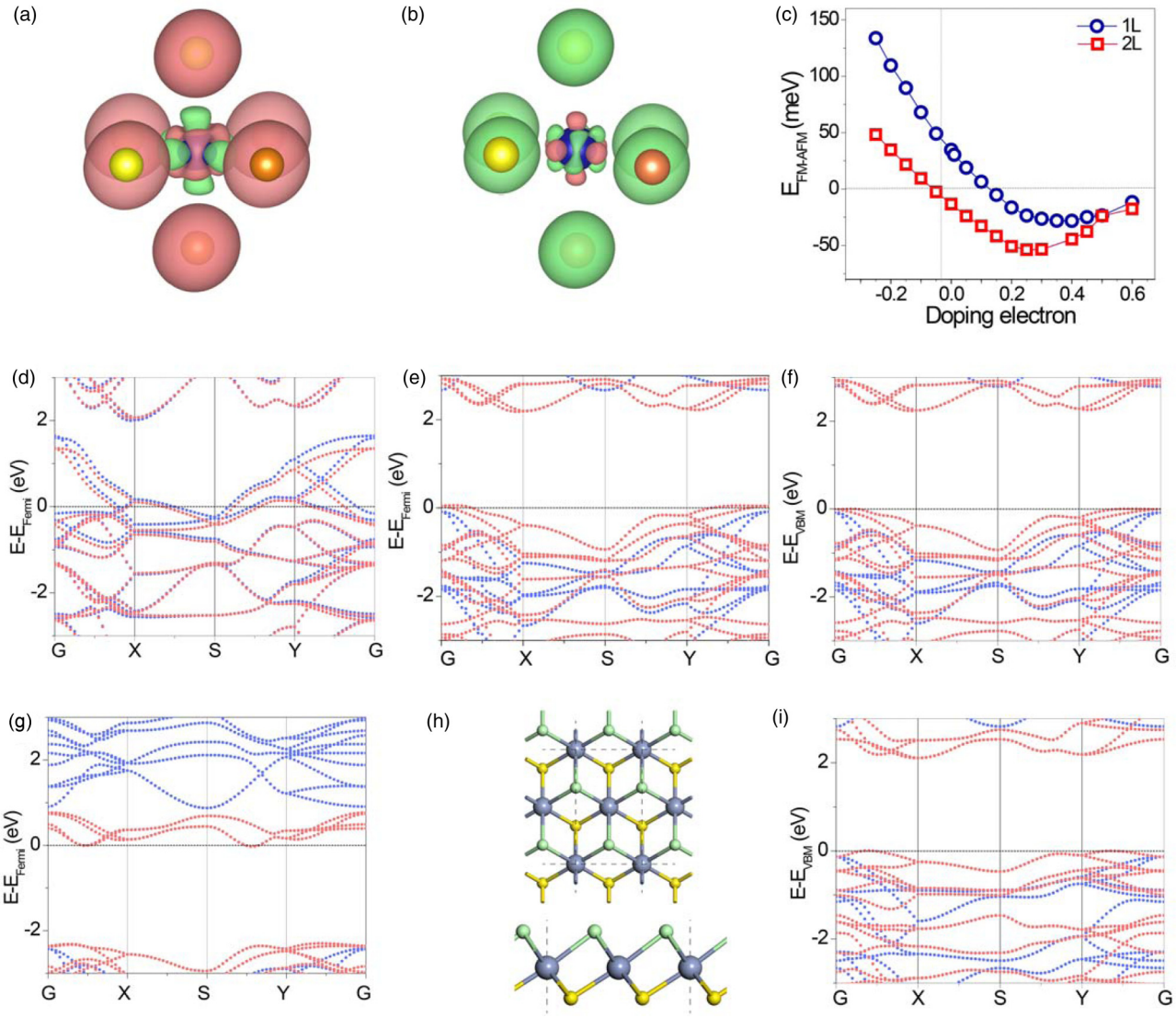

FIG. 4. Manipulation of in-plane magnetic ordering and electronic structure by electron and hole doping. (a), (b) Differential charge density of electron- or hole-doped monolayer CrS_2, respectively. (c) Energy difference between FM and sAFM intraplane magnetic orders with different doping concentrations. The blue and red symbols correspond to relative energy in mono- and bilayer, respectively. Doping a negative member of electrons represents doping a corresponding amount of holes. (d)–(g) Band structures of FM monolayer CrS_2 with different hole/electron doping concentrations: 0.20 h/S (d), 0.45 e/S (e), 0.50 e/S (f), and 0.60 e/S (g). (h) Top and side views of CrSCl Janus monolayer in the 1T phase. The light-green balls represent Cl atoms. (i) Electronic band structure of the CrSCl monolayer in the ferromagnetic ordering, showing an intrinsic FM semiconductor with an energy gap of 2.11 eV.

threefold symmetry is restored and the Cr-S bond lengths are all 2.38 Å.

The bilayer contains four S sublayers and two Cr layers. Figure 3(j) shows an interlayer differential charger density (DCD) with an isosurface value of 0.0005 e/Bohr^3. This value is over twice those used in plotting PtS_2 and MoS_2 in Ref. [32], suggesting a rather strong electronic hybridization between the second and third S sublayers (balls in orange). Apparent charge reduction (green) was found near these two sublayers, and charge accumulation (light-rose) occurs around the middle region of them (marked by the blue rectangle). It shows that a considerable portion of electrons are shared by those two S sublayers, weakening the existing intralayer Cr-S bonding. As a result, a noticeable charge transfer from e_g to t_{2g} orbitals is observable [Fig. 3(k)], resulting in a mixture of Cr^{4+} and Cr^{3+} in the bilayer, as schematically shown in Fig. 2(f). This state, together with delocalized S p orbitals and their resulting strong interlayer S-S hopping, favors the double-exchange mechanism, giving rise to a large J_2 and J_4 for ferromagnetic coupling.

The magnetic anisotropy energies (MAE) of 1L to 4L were considered by comparing the total energies with the magnetic moments parallel to five different vectors, **a**, **b**, **c**, **P**, and **I** (Supplemental Table S4 and Fig. S5 [58]). The found sAFM-FM transition is still valid in these noncollinear spin calculations. The easy magnetization axis oscillates between out- (odd number of layers) and in- (even) plane directions, although the differences among vectors **b**, **I**, and **P** are even smaller than 0.01 meV and are thus indistinguishable in 2L. Nevertheless, either **I** or **P** direction could be regarded as a

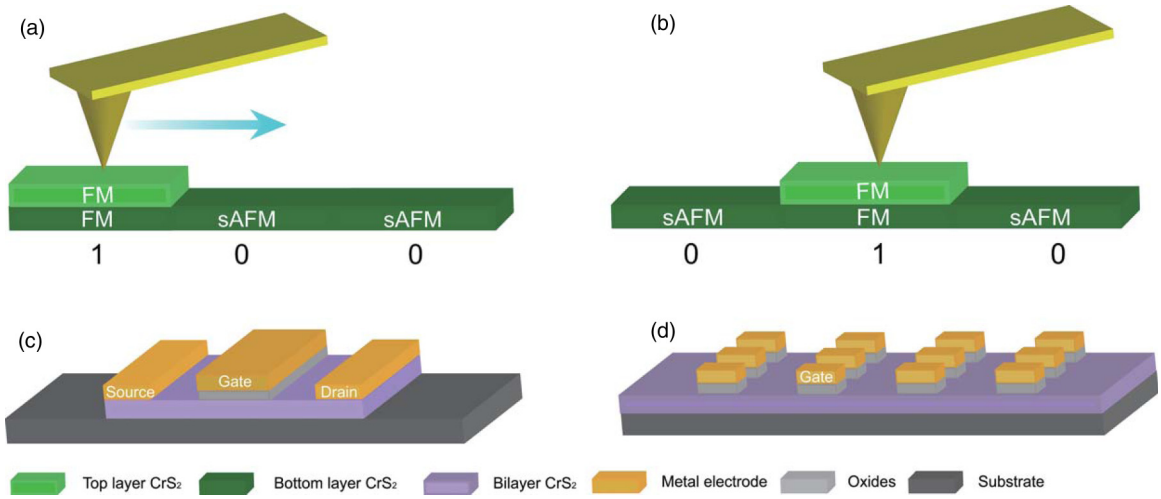

FIG. 5. Schematic drawing of a spin-logic application of few-layer CrS_2. (a), (b) Manipulation of mono- or bilayer CrS_2 flakes transiting between sAFM and FM states with sliding the top layer. (c) Spin-dependent transfer field-effect transistor controlled by injected charge from electric gates. (d) Magnetic logic array with every CrS_2 domain controlled by the corresponding electric gate.

tilted in-plane direction. Such oscillations most likely result from a confined quantum well state formed between top and bottom layers [70,71], as reported in Co few layers [72]. The band structure of the bilayer shows a metallic feature, but the E_F is slightly shifted by ~0.1 eV [Fig. 3(l)] compared to the monolayer case. In addition, the interlayer force constant of the bilayer was derived as 52.6×10^{18} and 33.7×10^{18} N/m^3 for the breathing and shear modes, similar to the values of the breathing mode of PtS_2 [32] and the shear mode of MoS_2 [73], respectively. In light of these results, CrS_2 appears as strongly electronic and magnetic but moderate mechanical interlayer couplings, which implies the feasibility of a tuning magnetism by electrically controlled charge manipulation.

D. Manipulation of in-plane magnetic ordering by charge doping

Direct charge doping using an ionic potential method [66] efficiently tunes magnetism in few-layer CrS_2 that n doping leads to an explicit e_g to t_{2g} charge transfer, as illustrated in a doping DCD of a monolayer [Fig. 4(a)]. A p-doping case shows an opposite pattern [Fig. 4(b)], implying that a FM-to-sAFM transition in the bilayer is inducible by p doping. Figure 4(c) plots the relative energies of sAFM and FM as a function of doping level for both mono- and bilayers. It shows p doping is always prone to make the sAFM ordering more favored, while n doping plays an opposite role. In the monolayer, an n-doping level of 0.13 e/S leads to both configurations being energetically degenerate. The largest energy differences of 25 and 54 meV are achieved at 0.35 and 0.25 e/S for mono- and bilayers, respectively. After these doping levels, the difference decreases and nearly vanishes at 0.5−0.6 e/S. These results, again, support the mixed-valence picture for double exchange. Ideally, the 0.25 e/S doping corresponds to the half-Cr^{3+} and half-Cr^{4+} case, which maximizes the double-exchange strength. For the level at 0.5 e/S, however, all Cr^{4+} were reduced to Cr^{3+}, which suppresses the double-exchange coupling. Charge doping also shifts the E_F which changes the monolayer from a heavily p-doped sAFM semiconductor to a half-metal, then an FM semiconductor with a band gap of 2.24 eV, and eventually to an n-type semiconductor [Figs. 4(d)–4(g)]. The bilayer shows a similar trend as shown in the Supplemental Material, Fig. S6 [58]. Another practical charge doping route lies in elemental substitution of S by Cl, as inspired by the recently synthesized Janus monolayers [46,47]. Figure 4(h) shows a CrSCl Janus monolayer where all S atoms in a sublayer are entirely replaced by Cl atoms. It is an intrinsic FM semiconductor with a band gap of 2.11 eV [Fig. 4(i)]. The FM state is energetically favored by at least 85 meV/Cr.

Since charge doping could tune both the mono- and the bilayers from heavily p-doped to n-doped semiconductors, we estimated phonon-limited mobilities for both hole and electron in CrS_2 mono- and bilayers (Table I). The hole mobilities of the two in-plane directions in both 1L and 2L are in hundreds of cm^2/V s, comparable with those of BP. The electron mobilities are generally larger than hole mobilities, especially the electron mobility of 2L CrS_2 of over 10 000 cm^2/V s in both in-plane directions. The conduction band of CrS_2 layers is comprised of Cr d_{z^2} orbitals, which is less affected by the in-plane structural deformation. This feature, therefore, leads to a rather small deformation potential for electrons, giving rise to high electron mobilities.

E. Proposed devices

In light of this discussion, there are diverse possibilities to manipulate CrS_2 few layers transiting between sAFM and FM states, which could be employed in magnetic data recording and information processing with the manipulation by, e.g., sliding of the second layer [Figs. 5(a) and 5(b)] and electric field [Figs. 5(c) and 5(d)]. As illustrated in Figs. 5(a) and 5(b), the stacking of an additional CrS_2 layer could, most likely, maintain the FM ordering locally. The sAFM and FM states, distinguishable with or without net magnetic moment, could be employed for data recording or processing, i.e., sAFM standing for bit "0" and FM for "1". In Fig. 5(a), we assume three bits which reads "100." However, they change to "010" if the second layer was moved from the left to the middle position by, e.g., an atomic force microscopy tip. Another route for charge doping

TABLE I. Phonon-limited electron/hole mobility of CrS_2 in 2H/1T phase, compared with MoS_2, $PtSe_2$ [37], and black phosphorus [12]. Here, m_x^* and m_y^* are carrier effective masses along the x and y directions, respectively; $E_{1x}(E_{1y})$, $C_{x\_2D}(C_{y\_2D})$, and $\mu_{x-2D}(\mu_{y-2D})$ are the deformation potentials, 2D elastic modulus, and the mobility along the x (y) direction, respectively.

Carrier type	Number of layers		m_x^*/m_0	m_y^*/m_0	m_d	C_{x_2D} (J/m^2)	C_{y_2D} (J/m^2)	E_{1x} (eV)	E_{1y} (eV)	μ_{x-2D} (10^3 cm^2/Vs)	μ_{y-2D} (10^3 cm^2/Vs)
		2H-CrS_2	0.90	0.84	0.87	117.57	117.91	4.28	4.57	0.17	0.17
		1T-CrS_2	1.15	0.72	0.91	73.43	63.84	0.71	2.23	2.31	0.53
	1L	MoS_2	0.47	0.47		129.93	135.34	5.57	5.55	0.41	0.43
e		$PtSe_2$	0.26	0.48		66.95	66.82	2.20	0.72	3.25	16.25
		BP	0.17	1.12	0.44	14.5	50.8	2.72	7.11	0.56	0.04
		2H-CrS_2	0.74	0.74	0.74	234.28	234.20	4.16	4.55	0.51	0.43
	2L	1T-CrS_2	0.33	0.49	0.40	93.82	92.02	1.05	0.70	16.46	16.71
		BP	0.18	1.13	0.45	28.74	97.31	5.02	7.35	0.30	0.07
		2H-CrS_2	0.90	0.84	0.87	117.57	117.57	2.41	2.14	0.53	0.78
	1L	1T-CrS_2	0.76	0.28	0.46	73.43	63.84	2.23	8.90	0.54	0.22
h		BP	0.15	6.35	0.98	14.47	50.80	2.50	0.15	0.33	7.71
		2H-CrS_2	2.74	2.40	2.57	234.28	234.20	1.43	1.31	0.29	0.46
	2L	1T-CrS_2	0.76	2.23	1.30	93.82	92.02	1.71	1.40	1.15	0.19
		BP	0.15	1.81	0.52	28.74	97.31	2.45	1.63	1.30	0.82

lies in electric field applied to shift chemical potentials of samples. Figure 5(c) shows a schematic diagram of a magnetic field-effect transistor where the gate voltage could tune the CrS_2 few layers switching between sAFM and FM states. Spin-polarized current thus flows differently in this device through two spin components if it maintains the FM state. In line with this idea, an array could be built as illustrated in Fig. 5(d). This array could be used as a data recording where each gate controls each bit switching between the FM (1) and sAFM (0) states.

IV. CONCLUSION

In summary, we show that intralayer magnetism is tunable by interlayer engineering, direct charge doping, and elemental substitution, as illustrated in CrS_2 few layers. In particular, an in-plane sAFM-to-FM transition occurs when the thickness increases from mono- to multilayers, where the interlayer coupling strongly favors FM ($J_4 = -10.8$ meV). The coexistence of Cr^{4+} and Cr^{3+} induced by interlayer charge sharing favors the FM in-plane coupling via a double-exchange coupling mechanism, which is confirmed by our calculations of the doped CrS_2 mono- and bilayers. The CrSCl Janus monolayer, an example of substitutional charge doping, was predicted to be an intrinsic FM semiconductor. Our results manifest that the interlayer coupling could, exceptionally, tune magnetic properties, in addition to its tunability of electronic [4,30–32,34], mechanical [4,30], vibrational [14], and optical [13,33] properties. This opens diverse possibilities to manipulate CrS_2 few layers transferring between sAFM and FM states, which could be employed in magnetic data recording and information processing, as proposed in prototypical devices (Fig. 5). Here, either layer stacking or charge doping changes intralayer magnetism, suggesting the magnetic interactions in both intra- and interlayer directions are still coupled even in the bilayer limit of CrS_2, a strong electronic coupling material. We would expect that the magnetic interactions may be decoupled for both directions in more weakly interacting bilayers. All these results allow us to manipulate magnetic long-range ordering through various routes, e.g., external electric gating, in two-dimensional materials, which shall boost magnetic applications of 2D materials in nanoelectronics, spintronics, and optoelectronics.

ACKNOWLEDGMENTS

The project was supported by the National Natural Science Foundation of China (Grants No. 11274380, No. 91433103, No. 11622437, and No. 61674171), the Fundamental Research Funds for the Central Universities, China, and the Research Funds of Renmin University of China (Grant No. 16XNLQ01). C.W. was supported by the Outstanding Innovative Talents Cultivation Funded Programs 2017 of Renmin University of China. Calculations were performed at the Physics Lab of High-Performance Computing of Renmin University of China.

[1] A. H. Castro Neto, F. Guinea, N. M. R. Peres, K. S. Novoselov, and A. K. Geim, The electronic properties of graphene, Rev. Mod. Phys. **81**, 109 (2009).

[2] A. K. Geim and K. S. Novoselov, The rise of graphene, Nat. Mater. **6**, 183 (2007).

[3] W. Han, R. K. Kawakami, M. Gmitra, and J. Fabian, Graphene spintronics, Nat. Nanotechnol. **9**, 794 (2014).

[4] J.-B. Wu, Z.-X. Hu, X. Zhang, W.-P. Han, Y. Lu, W. Shi, X.-F. Qiao, M. Ijiäs, S. Milana, W. Ji, A. C. Ferrari, and P.-H. Tan, Interface coupling in twisted multilayer graphene by resonant Raman spectroscopy of layer breathing modes, ACS Nano **9**, 7440 (2015).

[5] M. Chhowalla, H. S. Shin, G. Eda, L.-J. Li, K. P. Loh, and H. Zhang, The chemistry of two-dimensional layered

transition metal dichalcogenide nanosheets, Nat. Chem. **5**, 263 (2013).

[6] K. F. Mak, K. L. McGill, J. Park, and P. L. McEuen, The valley Hall effect in MoS_2: Transistors, Science **344**, 1489 (2014).

[7] S. Barja, S. Wickenburg, Z.-F. Liu, Y. Zhang, H. Ryu, M. M. Ugeda, Z. Hussain, Z.-X. Shen, S.-K. Mo, E. Wong, M. B. Salmeron, F. Wang, M. F. Crommie, D. F. Ogletree, J. B. Neaton, and A. Weber-Bargioni, Charge density wave order in 1D mirror twin boundaries of single-layer $MoSe_2$, Nat. Phys. **12**, 751 (2016).

[8] J. Lin, S. T. Pantelides, and W. Zhou, Vacancy-induced formation and growth of inversion domains in transition-metal dichalcogenide monolayer, ACS Nano **9**, 5189 (2015).

[9] H. Liu, L. Jiao, F. Yang, Y. Cai, X. Wu, W. Ho, C. Gao, J. Jia, N. Wang, H. Fan, W. Yao, and M. Xie, Dense Network of One-Dimensional Midgap Metallic Modes in Monolayer $MoSe_2$ and Their Spatial Undulations, Phys. Rev. Lett. **113**, 066105 (2014).

[10] H. Liu, A.T. Neal, Z. Zhu, Z. Luo, X. Xu, D. Tománek, and P. D. Ye, Phosphorene: An unexplored 2D semiconductor with a high hole mobility, ACS Nano **8**, 4033 (2014).

[11] L. Li, Y. Yu, G. J. Ye, Q. Ge, X. Ou, H. Wu, D. Feng, X. H. Chen, and Y. Zhang, Black phosphorus field-effect transistors, Nat. Nanotechnol. **9**, 372 (2014).

[12] J. Qiao, X. Kong, Z.-X. Hu, F. Yang, and W. Ji, High-mobility transport anisotropy and linear dichroism in few-layer black phosphorus, Nat. Commun. **5**, 4475 (2014).

[13] Q. Jia, X. Kong, J. Qiao, and W. Ji, Strain- and twist-engineered optical absorption of few-layer black phosphorus, Sci. China Ser. G **59**, 696811 (2016).

[14] Z.-X. Hu, X. Kong, J. Qiao, B. Normand, and W. Ji, Interlayer electronic hybridization leads to exceptional thickness-dependent vibrational properties in few-layer black phosphorus, Nanoscale **8**, 2740 (2016).

[15] N. Mao, J. Tang, L. Xie, J. Wu, B. Han, J. Lin, S. Deng, W. Ji, H. Xu, K. Liu, L. Tong, and J. Zhang, Optical anisotropy of black phosphorus in the visible regime, J. Am. Chem. Soc. **138**, 300 (2016).

[16] O. V. Yazyev and L. Helm, Defect-induced magnetism in graphene, Phys. Rev. B **75**, 125408 (2007).

[17] H. González-Herrero, J. M. Gómez-Rodríguez, P. Mallet, M. Moaied, J. J. Palacios, C. Salgado, M. M. Ugeda, J.-Y. Veuillen, F. Yndurain, and I. Brihuega, Atomic-scale control of graphene magnetism by using hydrogen atoms, Science **352**, 437 (2016).

[18] K. M. McCreary, A. G. Swartz, W. Han, J. Fabian, and R. K. Kawakami, Magnetic Moment Formation in Graphene Detected by Scattering of Pure Spin Currents, Phys. Rev. Lett. **109**, 186604 (2012).

[19] B. Uchoa, V. N. Kotov, N. M. R. Peres, and A. H. Castro Neto, Localized Magnetic States in Graphene, Phys. Rev. Lett. **101**, 026805 (2008).

[20] J. Zhou, Q. Wang, Q. Sun, X. S. Chen, Y. Kawazoe, and P. Jena, Ferromagnetism in semihydrogenated graphene sheet, Nano Lett. **9**, 3867 (2009).

[21] C. Zhao, C. Jin, J. Wu, and W. Ji, Magnetism in molybdenum disulphide monolayer with sulfur substituted by 3d transition metals, J. Appl. Phys. **120**, 144305 (2016).

[22] R. R. Nair, M. Sepioni, I. L. Tsai, O. Lehtinen, J. Keinonen, A. V. Krasheninnikov, T. Thomson, A. K. Geim, and I. V. Grigorieva, Spin-half paramagnetism in graphene induced by point defects, Nat. Phys. **8**, 199 (2012).

[23] J. Cervenka, M. I. Katsnelson, and C. F. J. Flipse, Room-temperature ferromagnetism in graphite driven by two-dimensional networks of point defects, Nat. Phys. **5**, 840 (2009).

[24] J. Jung, T. Pereg-Barnea, and A. H. MacDonald, Theory of Interedge Superexchange in Zigzag Edge Magnetism, Phys. Rev. Lett. **102**, 227205 (2009).

[25] O. Hod, V. Barone, J. E. Peralta, and G. E. Scuseria, Enhanced half-metallicity in edge-oxidized zigzag graphene nanoribbons, Nano Lett. **7**, 2295 (2007).

[26] N. D. Mermin and H. Wagner, Absence of Ferromagnetism or Antiferromagnetism in One- or Two-Dimensional Isotropic Heisenberg Models, Phys. Rev. Lett. **17**, 1133 (1966).

[27] B. Huang, G. Clark, E. Navarro-Moratalla, D. R. Klein, R. Cheng, K. L. Seyler, D. Zhong, E. Schmidgall, M. A. McGuire, D. H. Cobden, W. Yao, D. Xiao, P. Jarillo-Herrero, and X. Xu, Layer-dependent ferromagnetism in a van der Waals crystal down to the monolayer limit, Nature (London) **546**, 270 (2017).

[28] M. A. McGuire, H. Dixit, V. R. Cooper, and B. C. Sales, Coupling of crystal structure and magnetism in the layered, ferromagnetic insulator CrI_3, Chem. Mater. **27**, 612 (2015).

[29] C. Gong, L. Li, Z. Li, H. Ji, A. Stern, Y. Xia, T. Cao, W. Bao, C. Wang, Y. Wang, Z. Q. Qiu, R. J. Cava, S. G. Louie, J. Xia, and X. Zhang, Discovery of intrinsic ferromagnetism in two-dimensional van der Waals crystals, Nature (London) **546**, 265 (2017).

[30] K. Liu, L. Zhang, T. Cao, C. Jin, D. Qiu, Q. Zhou, A. Zettl, P. Yang, S. G. Louie, and F. Wang, Evolution of interlayer coupling in twisted molybdenum disulfide bilayers, Nat. Commun. **5**, 4966 (2014).

[31] C. Zhang, C.-P. Chuu, X. Ren, M.-Y. Li, L.-J. Li, C. Jin, M.-Y. Chou, and C.-K. Shih, Interlayer couplings, Moiré patterns, and 2D electronic superlattices in MoS_2/WSe_2 heterobilayers, Sci. Adv. **3**, e1601459 (2017).

[32] Y. Zhao, J. Qiao, P. Yu, Z. Hu, Z. Lin, S.P. Lau, Z. Liu, W. Ji, and Y. Chai, Extraordinarily strong interlayer interaction in 2D layered PtS_2, Adv. Mater. **28**, 2399 (2016).

[33] H.-P. Komsa and A. V. Krasheninnikov, Electronic structures and optical properties of realistic transition metal dichalcogenide heterostructures from first principles, Phys. Rev. B **88**, 085318 (2013).

[34] P.-C. Yeh, W. Jin, N. Zaki, J. Kunstmann, D. Chenet, G. Arefe, J. T. Sadowski, J. I. Dadap, P. Sutter, J. Hone, and R. M. Osgood, Direct measurement of the tunable electronic structure of bilayer MoS_2 by interlayer twist, Nano Lett. **16**, 953 (2016).

[35] H. Kasai, K. Tolborg, M. Sist, J. Zhang, V. R. Hathwar, M. Ø. Filsø, S. Cenedese, K. Sugimoto, J. Overgaard, E. Nishibori, and B. B. Iversen, X-ray electron density investigation of chemical bonding in van der Waals materials, Nat. Mater. **17**, 249 (2018).

[36] J. Qiao, Y. Pan, F. Yang, C. Wang, Y. Chai, and W. Ji, Few-layer tellurium, One-dimensional-like layered elementary semiconductor with striking physical properties, Sci. Bull. **63**, 159 (2018).

[37] Y. Zhao, J. Qiao, Z. Yu, P. Yu, K. Xu, P. Lau Shu, W. Zhou, Z. Liu, X. Wang, W. Ji, and Y. Chai, High-electron-mobility and air-stable 2D layered $PtSe_2$ FETs, Adv. Mater. **29**, 1604230 (2017).

[38] X. Qiu and W. Ji, Illuminating interlayer interactions, Nat. Mater. **17**, 211 (2018).

[39] H.-B. Li, N. Lu, Q. Zhang, Y. Wang, D. Feng, T. Chen, S. Yang, Z. Duan, Z. Li, Y. Shi, W. Wang, W.-H. Wang, K. Jin, H. Liu, J. Ma, L. Gu, C. Nan, and P. Yu, Electric-field control of ferromagnetism through oxygen ion gating, Nat. Commun. **8**, 2156 (2017).

[40] H. L. Zhuang, M. D. Johannes, M. N. Blonsky, and R. G. Hennig, Computational prediction and characterization of single-layer CrS_2, Appl. Phys. Lett. **104**, 022116 (2014).

[41] J. Zhang, H. Zheng, R. Han, X. Du, and Y. Yan, Tuning magnetic properties of CrS_2 monolayer by doping transition metal and alkaline-earth atoms, J. Alloys Compd. **647**, 75 (2015).

[42] C. Ataca, H. Şahin, and S. Ciraci, Stable, single-layer MX2 transition-metal oxides and dichalcogenides in a honeycomb-like structure, J. Phys. Chem. C **116**, 8983 (2012).

[43] S. Lebègue, T. Björkman, M. Klintenberg, R. M. Nieminen, and O. Eriksson, Two-Dimensional Materials from Data Filtering and *Ab Initio* Calculations, Phys. Rev. X **3**, 031002 (2013).

[44] S. Sinn, C. H. Kim, B. H. Kim, K. D. Lee, C. J. Won, J. S. Oh, M. Han, Y. J. Chang, N. Hur, H. Sato, B.-G. Park, C. Kim, H.-D. Kim, and T. W. Noh, Electronic structure of the Kitaev material α-$RuCl_3$ probed by photoemission and inverse photoemission spectroscopies, Sci. Rep. **6**, 39544 (2016).

[45] X. Wu, Y. Cai, Q. Xie, H. Weng, H. Fan, and J. Hu, Magnetic ordering and multiferroicity in MnI_2, Phys. Rev. B **86**, 134413 (2012).

[46] A.-Y. Lu, H. Zhu, J. Xiao, C.-P. Chuu, Y. Han, M.-H. Chiu, C.-C. Cheng, C.-W. Yang, K.-H. Wei, Y. Yang, Y. Wang, D. Sokaras, D. Nordlund, P. Yang, D. A. Muller, M.-Y. Chou, X. Zhang, and L.-J. Li, Janus monolayers of transition metal dichalcogenides, Nat. Nanotechnol. **12**, 744 (2017).

[47] J. Zhang, S. Jia, I. Kholmanov, L. Dong, D. Er, W. Chen, H. Guo, Z. Jin, V. B. Shenoy, L. Shi, and J. Lou, Janus monolayer transition-metal dichalcogenides, ACS Nano **11**, 8192 (2017).

[48] P. E. Blöchl, Projector augmented-wave method, Phys. Rev. B **50**, 17953 (1994).

[49] G. Kresse and J. Furthmüller, Efficient iterative schemes for *ab initio* total-energy calculations using a plane-wave basis set, Phys. Rev. B **54**, 11169 (1996).

[50] J. Klimeš, D. R. Bowler, and A. Michaelides, Van der Waals density functionals applied to solids, Phys. Rev. B **83**, 195131 (2011).

[51] I. A. Vladimir, F. Aryasetiawan, and A. I. Lichtenstein, First-principles calculations of the electronic structure and spectra of strongly correlated systems: The LDA + U method, J. Phys.: Condens. Matter **9**, 767 (1997).

[52] I. V. Solovyev, P. H. Dederichs, and V. I. Anisimov, Corrected atomic limit in the local-density approximation and the electronic structure of d impurities in Rb, Phys. Rev. B **50**, 16861 (1994).

[53] M. Cococcioni and S. de Gironcoli, Linear response approach to the calculation of the effective interaction parameters in the LDA + U method, Phys. Rev. B **71**, 035105 (2005).

[54] B.-T. Wang, W. Yin, W.-D. Li, and F. Wang, First-principles study of pressure-induced phase transition and electronic property of $PbCrO_3$, J. Appl. Phys. **111**, 013503 (2012).

[55] M. Aykol and C. Wolverton, Local environment dependent GGA + U method for accurate thermochemistry of transition metal compounds, Phys. Rev. B **90**, 115105 (2014).

[56] A. Jain, G. Hautier, S. P. Ong, C. J. Moore, C. C. Fischer, K. A. Persson, and G. Ceder, Formation enthalpies by mixing GGA and GGA + U calculations, Phys. Rev. B **84**, 045115 (2011).

[57] M. Korotin, V. Anisimov, D. Khomskii, and G. Sawatzky, CrO: A Self-Doped Double Exchange Ferromagnet, Phys. Rev. Lett. **80**, 4305 (1998).

[58] See Supplemental Material at http://link.aps.org/supplemental/10.1103/PhysRevB.97.245409 for more information about the theoretical methods and data analysis.

[59] J. Sugiyama, H. Nozaki, I. Umegaki, T. Uyama, K. Miwa, J. H. Brewer, S. Kobayashi, C. Michioka, H. Ueda, and K. Yoshimura, Static magnetic order on the metallic triangular lattice in $CrSe_2$ detected by μ^+SR, Phys. Rev. B **94**, 014408 (2016).

[60] J. Rouxel, A. Meerschaut, and G. A. Wiegers, Chalcogenide misfit layer compounds, J. Alloys Compd. **229**, 144 (1995).

[61] C. M. Fang, C. F. v. Bruggen, R. A. d. Groot, G. A. Wiegers, and C. Haas, The electronic structure of the metastable layer compound, J. Phys.: Condens. Matter **9**, 10173 (1997).

[62] S. Takagi, A. Toriumi, M. Iwase, and H. Tango, On the universality of inversion layer mobility in Si MOSFET's: Part II. Effects of surface orientation, IEEE Trans. Electron Devices **41**, 2363 (1994).

[63] G. Fiori and G. Iannaccone, Multiscale modeling for graphene-based nanoscale transistors, Proc. IEEE **101**, 1653 (2013).

[64] P. Kang, V. Michaud-Rioux, X. H. Kong, G. H. Yu, and H. Guo, Calculated carrier mobility of h-BN/γ -InSe/h-BN van der Waals heterostructures, 2D Mater. **4**, 045014 (2017).

[65] P. Kang, W.-T. Zhang, V. Michaud-Rioux, X.-H. Kong, C. Hu, G.-H. Yu, and H. Guo, Moiré impurities in twisted bilayer black phosphorus: Effects on the carrier mobility, Phys. Rev. B **96**, 195406 (2017).

[66] W. Ji, Z.-Y. Lu, and H. Gao, Electron Core-Hole Interaction and Its Induced Ionic Structural Relaxation in Molecular Systems under X-Ray Irradiation, Phys. Rev. Lett. **97**, 246101 (2006).

[67] J. L. Verble, T. J. Wietling, and P. R. Reed, Rigid-layer lattice vibrations and van der Waals bonding in hexagonal MoS_2, Solid State Commun. **11**, 941 (1972).

[68] S. Baroni, S. de Gironcoli, A. Dal Corso, and P. Giannozzi, Phonons and related crystal properties from density-functional perturbation theory, Rev. Mod. Phys. **73**, 515 (2001).

[69] H. Fang, C. Battaglia, C. Carraro, S. Nemsak, B. Ozdol, J. S. Kang, H. A. Bechtel, S. B. Desai, F. Kronast, A. A. Unal, G. Conti, C. Conlon, G. K. Palsson, M. C. Martin, A. M. Minor, C. S. Fadley, E. Yablonovitch, R. Maboudian, and A. Javey, Strong interlayer coupling in van der Waals heterostructures built from single-layer chalcogenides, Proc. Natl. Acad. Sci. USA **111**, 6198 (2014).

[70] M. Przybylski, M. Dąbrowski, U. Bauer, M. Cinal, and J. Kirschner, Oscillatory magnetic anisotropy due to quantum well states in thin ferromagnetic films, J. Appl. Phys. **111**, 07C102 (2012).

[71] J. Li, G. Chen, Y. Z. Wu, E. Rotenberg, and M. Przybylski, Quantum well states and oscillatory magnetic anisotropy in ultrathin Fe films, IEEE Trans. Magn. **47**, 1603 (2011).

[72] H. Yang, A. D. Vu, A. Hallal, N. Rougemaille, J. Coraux, G. Chen, A. K. Schmid, and M. Chshiev, Anatomy and giant enhancement of the perpendicular magnetic anisotropy of cobalt–graphene heterostructures, Nano Lett. **16**, 145 (2016).

[73] Y. Zhao, X. Luo, H. Li, J. Zhang, P. T. Araujo, C. K. Gan, J. Wu, H. Zhang, S. Y. Quek, M. S. Dresselhaus, and Q. Xiong, Interlayer breathing and shear modes in few-trilayer MoS_2 and WSe_2, Nano Lett. **13**, 1007 (2013).